

GT2011-46723

3D RANS Prediction of Gas-Side Heat Transfer Coefficients on Turbine Blade and Endwall

Jiang Luo, Eli H. Razinsky and Hee-Koo Moon
Solar Turbines Incorporated
A Caterpillar Company
San Diego, CA, USA

ABSTRACT

This paper presents a study using 3D computational fluid dynamics (CFD) based on Reynolds-averaged Navier-Stokes (RANS) equations to predict turbine gas-side heat transfer coefficients (HTC) on the entire airfoil and endwall. The CFD results at different spanwise sections and endwall have been compared with the flat-plate turbulent boundary layer correlation and with the data in a NASA turbine rotor passage with strong secondary flows, under three different flow conditions. The enhancement effects of secondary flow vortices on the blade surface and endwall heat transfer rate have been examined in detail. Analyses were conducted for the impact of Reynolds number and exit Mach number on heat transfer. The SST, $k-\epsilon$, $V2F$, and realizable $k-\epsilon$ turbulence models have been assessed. The classical log-law wall-functions have been found to be comparable to the wall-integration methods, but with much reduced sensitivity to inlet turbulence conditions. The migration of hot gas was simulated with a radial profile of inlet temperature. CFD results for mid-span HTCs of two other airfoils were also compared with test data. Overall results are encouraging and indicate improved HTC and temperature predictions from 3D CFD could help optimize the design of turbine cooling schemes.

INTRODUCTION

With turbine inlet temperature profiles flattened in recent combustor designs, the cooling of gas-producer turbine airfoil endwalls has become more important. But it is complicated by the 3D secondary flows and vortices, which cause enhanced heat transfer and large local variation. The 3D endwall flow and thermal field is very complex with separation, stagnation, multiple vortices of varying intensities and strong pressure gradients, as reviewed by Simon and Piggush [1] and studied by many researchers [e.g., 1-5]. Thus, accurate prediction of turbine gas-side heat transfer, especially the detailed distribution

in the endwall regions is essential to creating improved turbine designs that operate with higher turbine rotor inlet temperature, reduced cooling flow penalties, improved performance and component life [1].

RANS CFD techniques have been used to predict the loadings and flow distributions of blade rows, including endwall regions for over two decades [1, 6]. Dunn [6] reviewed in 2001 that CFD achieved only limited success in predicting turbine heat transfer, mainly due to the limitation of modeling turbulence and vortices, uncertainty of boundary conditions, and the inherent flow unsteadiness in turbomachinery. Much progress has been made in applying RANS CFD to turbine blade and endwall HTC in recent years (e.g., [7-13]). Various turbulence models with different wall treatments have been evaluated. A limiter of time scale was shown [7] to substantially improve the predictive accuracy for mid-span turbine HTC over the standard $k-\epsilon$ or $k-\omega$ models. Overall good or fair agreement was observed between 3D RANS predictions and data for HTC on a one and 1/2 stage turbine airfoil and endwall under engine realistic conditions [13].

Despite the progress, there still appears to be a lack of consistent accuracy using RANS CFD for HTC. Routine prediction of turbine HTC in the design environment is still often decoupled from prediction of aerodynamics. The external HTC values are often obtained from the correlation of the flat-plate turbulent boundary layer (TBL), usually with a test factor, or 2D boundary layer codes, e.g., TEXSTAN [14], rather than directly from 3D CFD. While such tools may be applicable near the mid-span, they are not accurate or valid near the endwalls and corners where the flow is highly 3D and dominated by secondary flows [1, 6]. Also in contrast to the multiple solutions at different radial sections (for pressure and suction sides) and on the endwalls as required by the current 1D/2D tools, a single 3D CFD solution can provide HTC and gas temperature in the entire blade passage.

Some discrepancy observed in CFD predictions of turbine heat transfer is actually related to the modeling of by-pass transition, especially when CFD solutions are compared with the data from cascade measurements. Accurate modeling of transition remains challenging even with the latest developments using additional equations for intermittency or new correlations [12, 15, 16]. The focus for the present paper is on modeling turbulent heat transfer since the tendency of turbine cooling designers is to be conservative and to assume fully turbulent flows over the gas-producer turbine airfoils [6].

There have been many efforts in predicting coupled fluid convection and solid conduction (conjugate heat transfer, CHT) which offers simultaneous solutions of aerodynamics and heat transfer in the hot gas and the internal cooling passages and the blade metal temperature [e.g., 17-18]. Recent CHT efforts include the film-cooled airfoils and an unsteady study [19]. For CHT to become feasible for design iterations, however, it is crucial to first achieve reliable and accurate HTC predictions since the CHT-predicted metal temperature depends strongly on its RANS-predicted HTC values.

To predict HTC on the entire airfoil and the endwalls and the local gas temperature distribution, 3D RANS is the only viable tool at this time. More efforts are needed to develop 3D RANS into a truly predictive and robust tool for HTC in a design environment. Hence the objectives of this paper include: 1) to develop a robust and reliable procedure with 3D RANS for improved accuracy of turbine HTC, especially near the endwalls; 2) to compare CFD predictions with test data and flat-plate correlations.

NUMERICAL METHOD

RANS CFD Solver

The RANS solver used is a commercial CFD package - STAR-CD V4.10, released in 2009 [20]. It solves the system of 3D RANS equations on unstructured meshes, with an implicit finite volume solver that employs a variant of the well-known SIMPLE algorithm for velocity-pressure correction. The convective fluxes in the mean-flow and turbulence equations are discretized with a second-order accurate differencing scheme called monotone advection and reconstruction (MARS). The convergence criteria (maximum residual tolerances) are set to 1×10^{-5} , for both flow and turbulence variables to ensure fully convergent solutions.

Turbulence Modeling

It is well known that the prediction of HTC is strongly affected by near-wall turbulence modeling. Typically there are two approaches: the wall-functions (WF, $y^+ \sim 30-100$) and wall-integration ($y^+ \sim 1$, also known as low-Reynolds-number functions - LRN). The wall-integration modeling may offer higher accuracy due to its resolution down to the viscous sublayer (albeit at higher cost). The wall functions,

using the classical logarithmic-law, essentially treat the boundary layer as fully turbulent. By bridging the viscous sub-layer and buffer layer, wall-functions avoid the need to employ a fine near-wall mesh, with associated computing overheads and/or convergence difficulty and have been used as a pragmatic approach since the early days of turbulence modeling. Although considered by some to be an "old method" and inferior to wall-integration, the wall-function approach is actually based on a solid theoretical foundation of turbulence theory and supported by measurements – the universal logarithmic-laws, as discussed by Durbin [21].

A number of turbulence closures have been evaluated, including: 1) the k- ϵ model with wall-function (KE_wf); 2) the shear-stress-transport model with wall-function (SST_wf) and with low-Reynolds-number functions (SST_lrn); 3) the realizable k- ϵ model with wall-function (RKE_wf) and 4) the V2F model which is a low-Reynolds-number model by default [20].

RESULTS and DISCUSSION

A transonic turbine rotor cascade, measured by Giel et al. in 1999 [4] at NASA Glenn, has been studied extensively, e.g. [9, 22]. This rotor blade is the focus for this paper due to its comprehensive HTC data on both the blade and endwall. CFD results were also obtained for the nozzles measured by Ames, et al. [23] and Hylton et al. [24], under different flow conditions. The aim is to assess RANS techniques with different wall-treatment methods and turbulence closures against the data from three different turbine airfoils.

Flow, Turbulence Conditions and CFD Model for 3D Rotor Cascade [4]

The NASA rotor blade [4] has flow conditions (M , Re , Tu) similar to typical industrial turbine conditions, with $M_2 = 1.0 - 1.4$, exit Re_2 varying from 1×10^6 to 2×10^6 . The axial chord $C_x = 127$ mm, true chord $C = 184.2$ mm, pitch = 130 mm, and span = 152.4 mm. Its design flow turning is 136° and inlet flow angle is 63.6° . Details of the test conditions are listed in Table 1 below.

Table 1 Flow Conditions for Test Cases

case	Re(Cx,in)	M(ex)	Tu (Grid)	M(in)	Re(Cx,ex)
2	5.00E+05	0.985	8% (yes)	0.345	9.99E+05
5	1.00E+06	1.322	8% (yes)	0.342	2.04E+06
6	1.01E+06	0.981	8% (yes)	0.339	2.04E+06

Only half of the linear turbine cascade is modeled due to its geometric symmetry. As in the measurement, the inlet total temperature T_{t1} was held as uniform at 288 K, without any spanwise variation, and the wall temperature was fixed at 321 K in the CFD runs. The inlet total pressure and exit (averaged) static pressure were specified per the test conditions. The inlet turbulent boundary layer

thickness (δ) on the endwall is 20 mm, about 26% of the half span (76.2 mm), which is modeled using the 1/7th power-law ($U/U_\delta = (y/\delta)^{1/7}$) at the CFD inlet.

Note the turbulence integral length scale L_x , as measured in experiments, is usually much larger than that in RANS codes, often defined with k and ϵ (or ω). The turbulence length scale in STAR-CD is defined as

$$L_t = C_\mu^{3/4} k^{1.5} / \epsilon = 0.164 k^{1.5} / \epsilon \quad (1)$$

with $C_\mu = 0.09$ (as in the k - ϵ model).

The streamwise turbulence integral length scale, L_x , reflects mainly the size of the largest energy-containing eddies in turbulent flows. An energy scale, L_k , representative of the average size of the energy-containing eddies [25], can be defined using k and ϵ for isotropic turbulence assumed downstream of the grids:

$$L_k = 1.5(2/3k)^{1.5} / \epsilon = 0.8165k^{1.5} / \epsilon \quad (2)$$

Equations (2) and (1) indicate the CFD length scale L_t is about 1/5 of L_k , i.e., $L_t \approx L_k/5$. The two length scales, L_x and L_k , representing the largest size and the average size of energy-containing eddies, should be on the same order [25]. Indeed, the measured L_x is roughly the same as L_k for grid turbulence [26]. If the assumption of $L_x \approx L_k$ is made for the grid turbulence in the current data sets, L_t may be specified to be roughly 1/5 of the integral scale L_x , i.e., $L_t \approx L_x/5$.

As in the measurement, the turbulence intensity Tu_1 was fixed at 8%, and the length scale was set to $L_t = 6$ mm, which is equivalent to the measured L_x of 29.2 mm per the assumption above. This results in a high eddy-to-molecular viscosity ratio at about 1,400 (for k - ϵ models) at the inlet, however. If L_t is set to be the same as L_x of 29.2 mm, the eddy-to-molecular viscosity ratio would be excessively high at about 7,000.

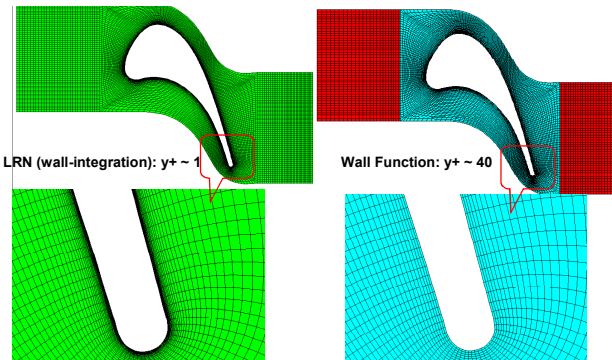


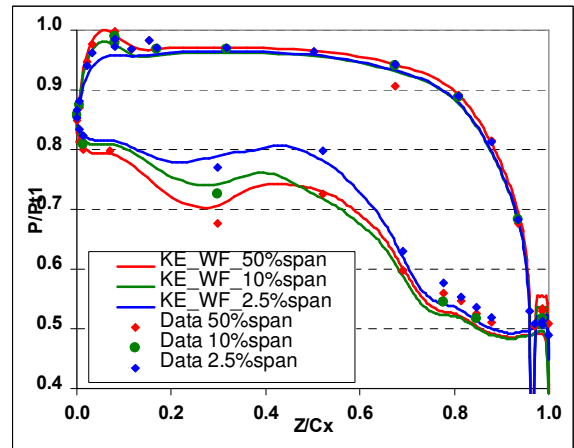
Fig. 1 Comparison of CFD mesh: wall-function (WF) vs. low-Reynolds-number (LRN)

The fine LRN mesh (with $y^+ \sim 1$) and "coarse" wall-function mesh ($y^+ \sim 40$) have been compared in Fig. 1. The

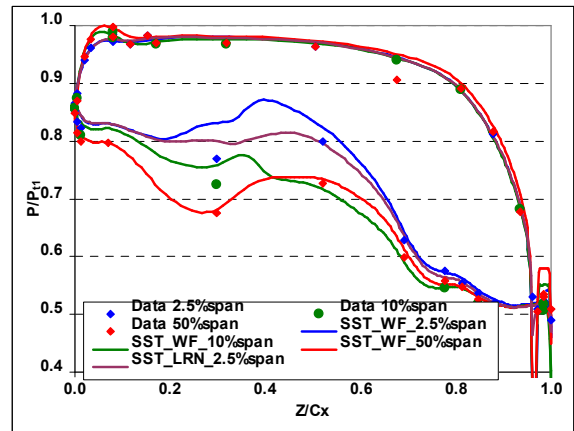
total WF mesh count is about 0.8 million for the half-span domain (1.6 million for full-span), with 11,300 blade-to-blade cells and 71 spanwise cells. There are 1.67 million cells for the LRN mesh (half-span), with 19,700 blade-to-blade cells and 85 spanwise cells. Internal mesh sensitivity study and external study (e.g., [22]) indicate these meshes have provided grid-independent solutions.

Results for Flow and Heat Transfer of Case #2 ($M_{ex} = 0.99$, $Re(C_{x,ex}) = 10^6$)

Pressure Loading and Flow Structure



a) k - ϵ with wall-function

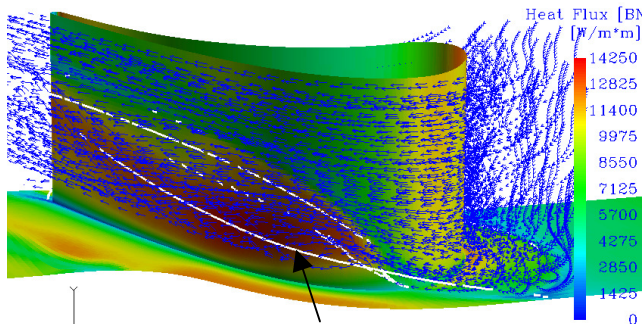


b) SST with wall-function and LRN

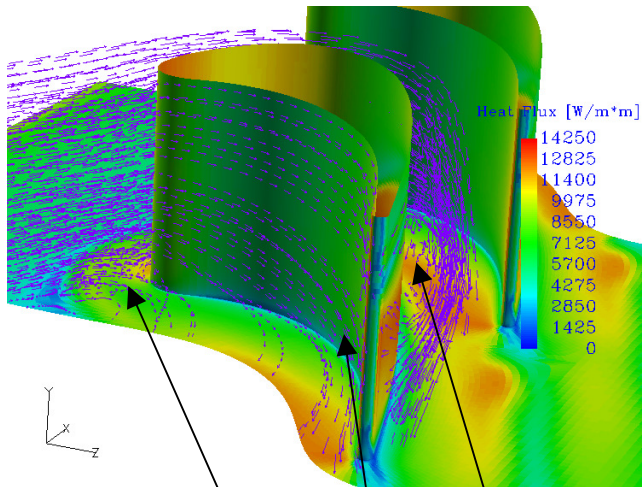
Fig. 2 CFD-predicted loading vs. data at three spanwise sections (50%, 10%, 2.5%, Case #2)

The predicted loading (P/P_{t1}) along the blade (Z/C_x) at different spanwise sections (50%, 10%, 2.5%) are shown in Fig. 2a (k - ϵ) and 2b (SST), in comparison with the data. All the predictions are in excellent agreement with the data on the pressure side which shows only slight variation along the span. It is known since mid 1980s [27] that 3D RANS can predict the reduced loading, caused by the secondary flow effects, on the suction side near the endwall. Indeed, the agreement in Fig. 2 is good or fair on

the suction side, where the deceleration near $Z/C_x = 0.3-0.5$ is also captured well. There are some differences between the $k-\epsilon_{wf}$ and the SST_{wf} results, with SST_{wf} showing a reduction of loading at 10% and 2.5% span larger than the data. This appears to be caused by the over-prediction of passage vortex size by the SST_{wf} model. The SST_{lrn} solution at 2.5% span showed some improvement over SST_{wf} .



a) Suction side view (vortex cores shown in white curves)



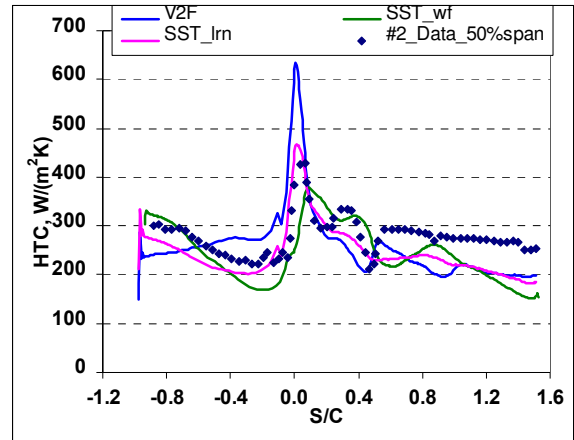
b) 2nd view (horseshoe vortex, downwash; passage vortex)
Fig. 3 Streamlines and secondary vortices (predicted by SST with wall-function) through the turbine passage (wall colored by heat flux)

Figure 3a shows the streamlines of the vortices developed inside the passage, with the walls colored by computed heat flux. The upstream endwall boundary layer thickness is only 26% of half-span, but the impact of the passage vortex extends to about 2/3 of half-span at the exit. A trailing-edge view in Fig. 3b shows the horseshoe vortex near the leading edge, the passage vortex roll-up near the suction side, the flow downwash near the pressure side and the crossflow near the platform, resulting in higher heat flux locally on the wall.

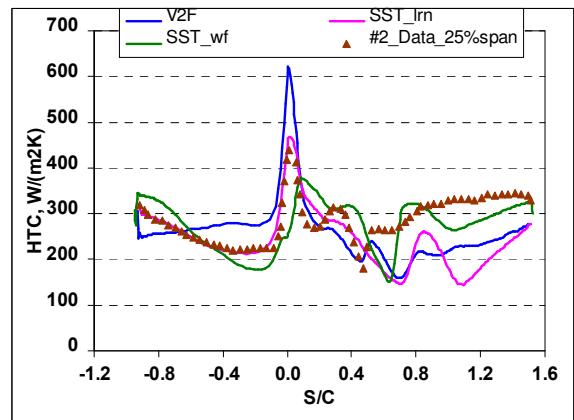
Impact of Near-Wall Treatment

Figure 4 shows the comparison of HTC solutions from the SST_{wf} , SST_{lrn} and V2F models for the Giel airfoil.

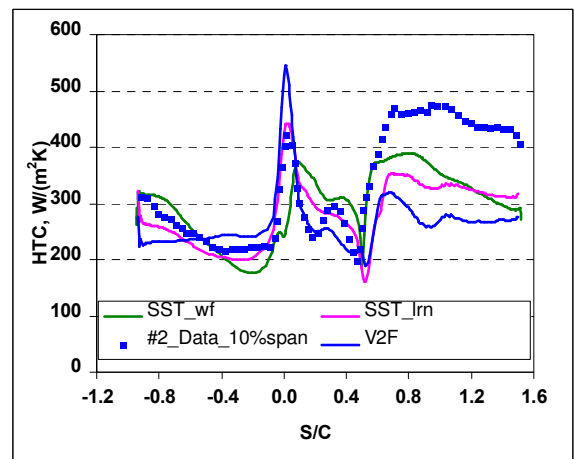
The suction side is on the right, from $S/C = 0$ to $S/C \sim 1.5$ and the pressure side is on the left where $S/C < 0.0$. The SST_{lrn} solution shows improvement over SST_{wf} near the leading edge and on the pressure side, but comparable or even lower accuracy in other regions.



a) 50% span ($S/C < 0$ pressure side; > 0 suction side)



b) 25% span



c) 10% span

Fig. 4 CFD-predicted HTC vs. data at three spanwise locations: impact of turbulence model and near-wall treatment (SST_{wf} , SST_{lrn} vs. V2F)

The prediction by the SST_wf model largely captures the elevated heat transfer due to secondary flow vortex (as in Fig. 3a, 3b) on the suction side at 25% span and is significantly better than the SST_lrn model. But both models under-predict the enhanced HTC on the suction side at 10% span where the data shows very high HTC that is higher than the leading edge HTC. Overall, the wall-function method appears to be more desirable than the wall-integration for the SST model, considering the saving in grids and the need for fast turnaround.

The V2F model has been shown to provide improved predictions of HTC over other models for some airfoils, especially when transition is present and a relatively small length scale is used at inlet [e.g., 16]. But it over-predicts HTC near the leading edge in Fig. 4. This is due to the excessive turbulence level in the domain, starting with $\mu_t/\mu = 2300$ at the inlet, which is higher than that in SST due to the difference in their eddy-viscosity formulas, under the same Tu_i and length scale. The V2F has largely under-predicted the HTC enhancement on the suction side at the three spanwise sections.

Effects of Inlet Turbulence Length Scale

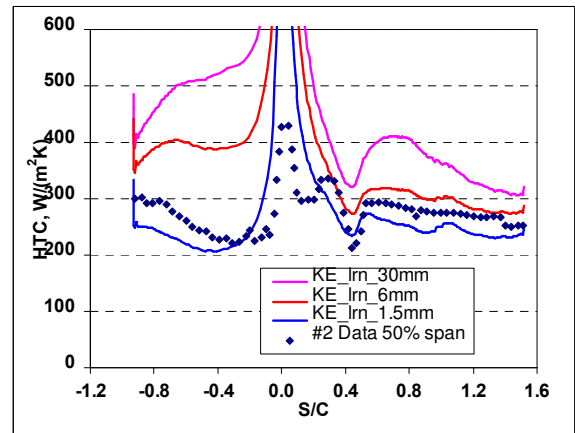
As discussed above, the measured turbulence integral length scale L_x , is often different from and much larger than that in RANS codes, often defined with k and ϵ (or ω). The inlet turbulence length scale was observed to impose a large impact on the predicted HTC by the V2F and LRN k- ϵ and other two-equation models [16, Fig. 5a], due to the "stagnation point anomaly" in those models which predict unphysically excessive turbulence amplification around the leading edge, especially when large length scales are specified at the inlet. The HTC values were significantly over-predicted near the leading edge and the pressure side by the LRN k- ϵ model with $L_t = 6$ mm and 30 mm. A reasonable solution is obtained when $L_t = 1.5$ mm which allows certain decay of freestream turbulence in the blade passage, as discussed in [16].

With the enforcement of log-law by the wall-function treatment at the wall, it is clear from Fig. 5b that the k- ϵ _wf predictions of HTC are not affected much by the inlet length scale, unlike the k- ϵ _lrn solutions. In other words, the log-law treatment at the wall reduces the sensitivity of HTC solutions to the specified inlet L_t and turbulence level calculated downstream.

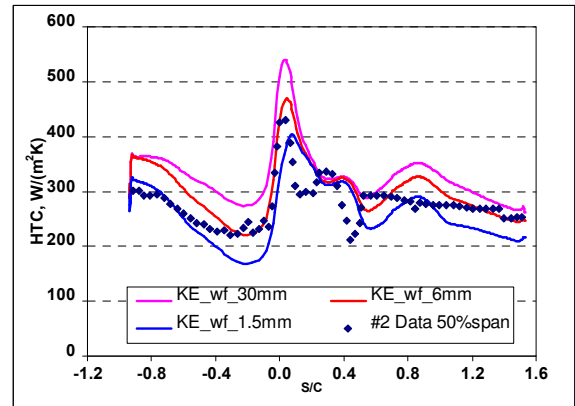
Predicted HTC and Stanton Number: Impact of Turbulence Modeling

The HTC predictions (by the SST, k- ϵ , and realizable k- ϵ models, all with wall-functions) vs. the flat-plate correlation and the data (Case #2) at the 50%, 25%, 10% span are shown in Fig. 6a, 6b, 6c, respectively. The flat-plate turbulent boundary layer (TBL) solution is based on

the classical correlation, $H_{TBL} = 0.0296 Pr^{1/3} Re_s^{0.8} K/S$ [14], which accounts for property variation through conductivity (K) and viscosity (ν) in Re_s .



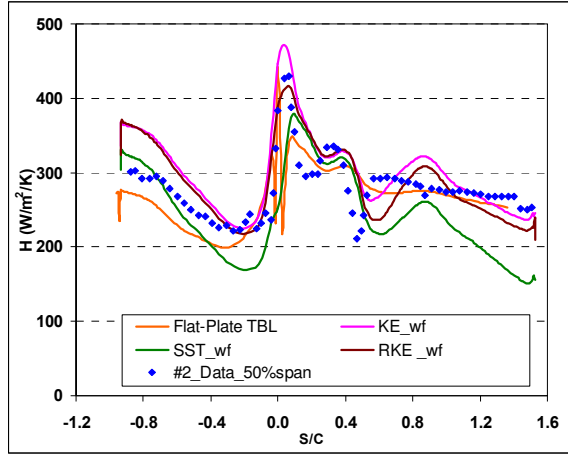
a) k- ϵ _lrn model



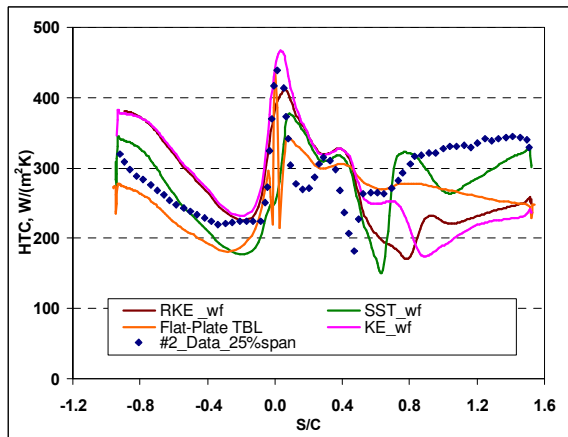
b) k- ϵ _wf model

Fig. 5 HTC predicted by k- ϵ _wf and k- ϵ _lrn models vs. data at mid-span (Case #2; $Tu_i=8\%$): impact of length scale and wall treatment

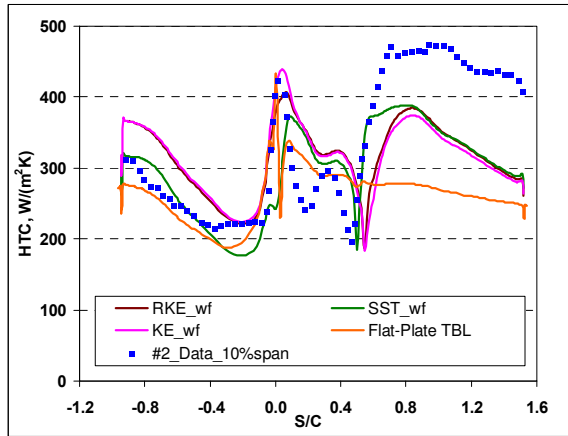
At the mid-span (Fig. 6a), the SST_wf solution on the pressure side (PS) is slightly lower than the KE_wf (k- ϵ) and the RKE_wf solutions, with all in agreement with the data and the flat-plate correlation. The close agreement between the data and flat-plate correlation on the suction side (SS), except the dip near $S/C = 0.47$, suggests an early boundary layer transition and it behaves like a flat-plate turbulent boundary layer afterwards. The RKE_wf solution is very close to the KE_wf solution and both agree well with the data, better than the SST solution, especially toward the SS trailing edge (TE). The under-prediction of heat transfer by the SST model on the rear suction side at the mid-span appears to be caused by its over-prediction of the passage vortex near the endwall.



a) 50% span



b) 25% span



c) 10% span

Fig. 6 Heat transfer coefficients predicted by the k-ε, realizable k-ε and SST models with wall-function vs. the data and flat-plate correlation at 50%, 25%, 10% span (Case #2)

At 25% span (Fig. 6b) and 10% span (Fig. 6c), while the data and predictions for the pressure side remain very similar to those at 50% span, there is a significant increase in HTC data on the suction side. This enhancement of HTC is caused by the passage vortex which exerts

impingement-like influence on the local heat flux (Fig. 3b). As the enhancement is from 3D flows, it is not surprising that the flat-plate correlation totally missed it. By modeling the 3D secondary flows, the CFD solutions, especially with the SST model, largely capture the HTC enhancement. The SST solution represents a major improvement over the correlations at both sections (Fig. 6b and 6c).

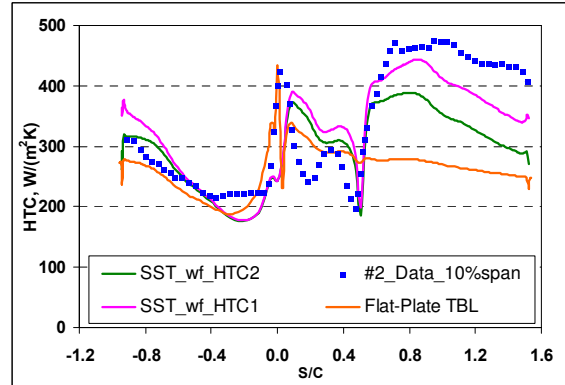


Fig. 7 Impact of the definitions of HTC ($HTC_1 = \dot{Q}_w / (T_{t1} - T_w)$, $HTC_2 = \dot{Q}_w / (T_{aw} - T_w)$) on the predictions (by the SST model with wall-function; 10% span of Case #2)

The impact of the definitions of HTC is shown in Fig. 7. The HTC_2 (in the data) employs the wall adiabatic recovery temperature in its definition (T_{aw} in Nomenclature), i.e., $HTC_2 = \dot{Q}_w / (T_{aw} - T_w)$, while $HTC_1 = \dot{Q}_w / (T_{t1} - T_w)$. HTC_2 is similar to HTC_1 except in the high-Mach number region. The difference of HTC_1 and HTC_2 is significant on the rear suction side, which is amplified by the small difference of T_{t1} and T_w in the current case.

The SST-predicted Stanton number ($St \times 1000$) is compared to the data on the endwall in Fig. 8. The CFD prediction agrees favorably with the data. It clearly captures the elevated heat transfer near the leading edge, mainly caused by the horse-shoe vortex. For some reason, the CFD solution shows the peak heat transfer on the suction side near the leading edge, while the data shows the peak right at the leading edge. CFD also captures the enhanced level near the pressure side, due to the downwash of secondary flow there. It is not possible for the flat-plate correlation to predict such enhancements caused by 3D effects. Note the predicted contour of $St \times 1000$ is derived from HTC_1 (because STAR-CD can only output HTC_1), but the data is from HTC_2 . Some difference between the prediction and data is due to the difference between HTC_1 and HTC_2 (Fig. 7), particularly towards the passage exit.

Figure 9 shows that $St \times 1000$ predicted by the SST model is in favorable agreement with the data on the entire blade. The SST prediction captured high heat transfer near the leading edge and also the increase on the suction side

caused by the passage vortex roll-up. Again the prediction is shown in HTC_1 and the measurement is from HTC_2 , which contributes partially to the difference between the prediction and data toward the trailing edge.

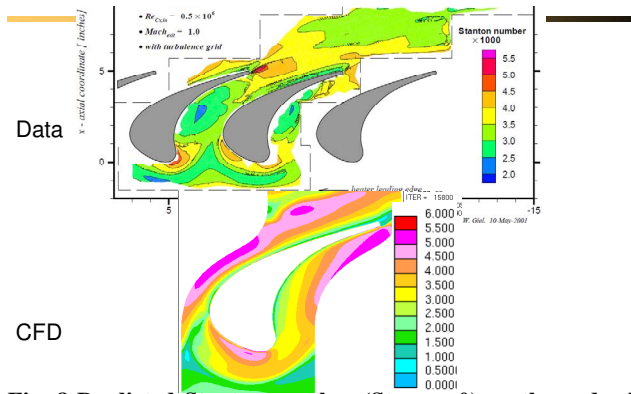


Fig. 8 Predicted Stanton number ($St \times 1000$) on the endwall (by SST model with wall-function) compared with data

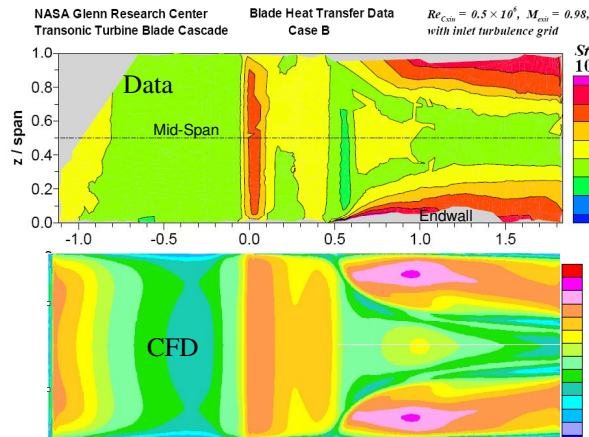


Fig. 9 Predicted Stanton number ($St \times 1000$) on the blade (by SST model with wall-function) in comparison to data

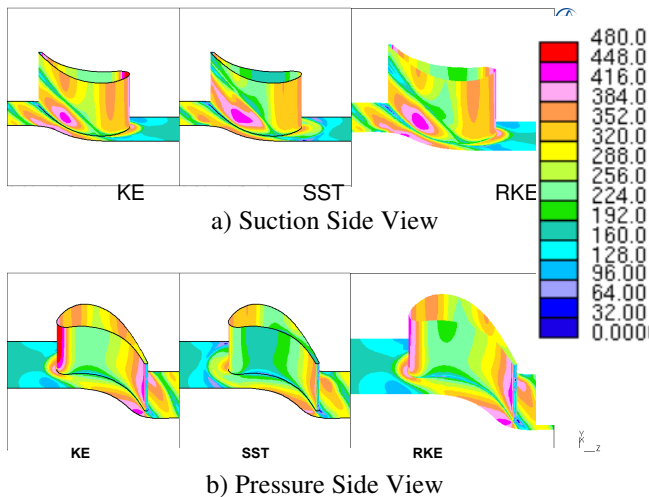


Fig. 10 CFD-predicted HTC on the blade and endwall: effects of turbulence modeling

The HTC contours predicted by different turbulence models (k- ϵ , Realizable k- ϵ and SST) are shown in Fig. 10. While there is some difference among the predictions, they all show the enhanced heat transfer on the suction side, the endwall and near the leading edge by 3D secondary flow effects. It appears that the employment of wall functions has effectively reduced the sensitivity of HTC solutions to turbulence modeling, because the logarithmic-laws are enforced near the walls.

Impact of Reynolds Number (Case #6: $M_{ex} = 0.98$, $Re(C_x, ex) = 2 \times 10^6$)

The Reynolds number of Case #6 is twice of that in Case #2, with other flow conditions being identical. The CFD-predicted (with the SST and k- ϵ models) HTC vs. the flat-plate correlation and the data at the 50% span are shown in Fig. 11. At the 50% span, the flat-plate correlation under-predicts HTC on the pressure side where both CFD solutions show better accuracy. On the suction side, both CFD solutions show the wavy distribution of HTC, including the 2nd peak, with the k- ϵ solution showing better agreement than the SST solution.

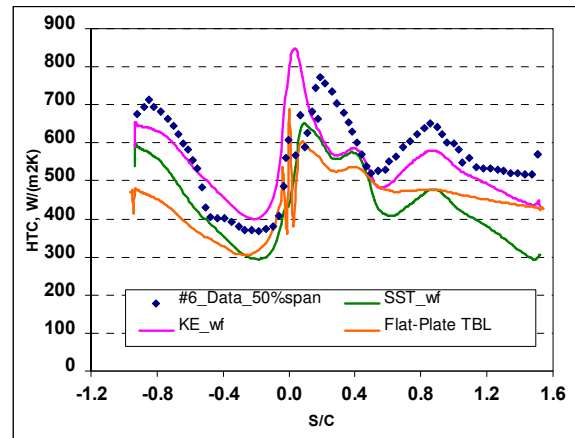
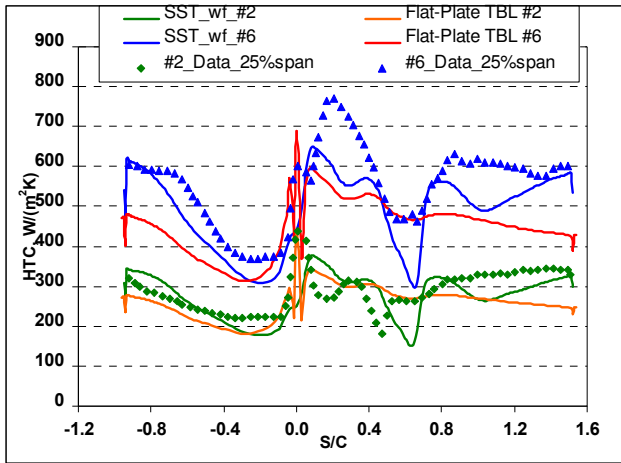
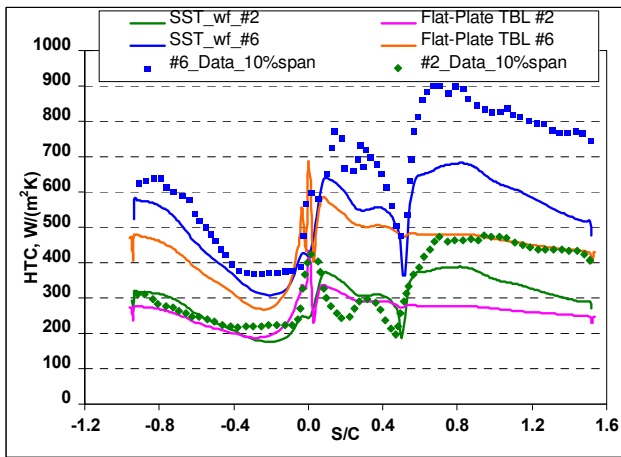


Fig. 11 HTC predicted by k- ϵ and SST with wall-function vs. flat-plate correlation and data at the 50% span (Case #6)

The isolated impact of Reynolds number on HTC at 25% and 10% span is presented in Fig. 12a, 12b, respectively, where the HTC of Case #6 is roughly doubled from that of Case #2. This has been captured well by the SST prediction, except some local variations. At both sections, the SST solutions again agree well with the data for the pressure side. A significant improvement is also evident on the suction side (Fig. 12b), due to the modeling of 3D secondary flows. Like Case #2, the large enhancement of HTC at 10% span on the suction side is under-predicted by CFD. The flat-plate correlation underestimates HTC on much of the airfoil surface at both 25% and 10% span for Case #6.



a) 25% span



b) 10% span

Fig. 12 SST-predicted HTC vs. flat-plate correlation and data at 25%, 10% span: Impact of Reynolds number (Case #2 vs. Case #6)

Impact of Mach Number (Case #5: $M_{ex} = 1.35$, $Re(C_{x,ex}) = 2 \times 10^6$)

To study the impact of Mach number on HTC, Case #5 was analyzed which has supersonic exit flow, with other conditions identical. The HTC predicted by the SST and k- ϵ models and the flat-plate correlation are compared with the data at 25% span in Fig. 13. As in Case #6, the CFD solutions capture the elevated HTC on the pressure side, better than the flat-plate correlation. On the suction side, the SST solution follows the wavy distribution as in the HTC data, including the second peak, which is missed by the flat-plate correlation and under-predicted by the k- ϵ solution.

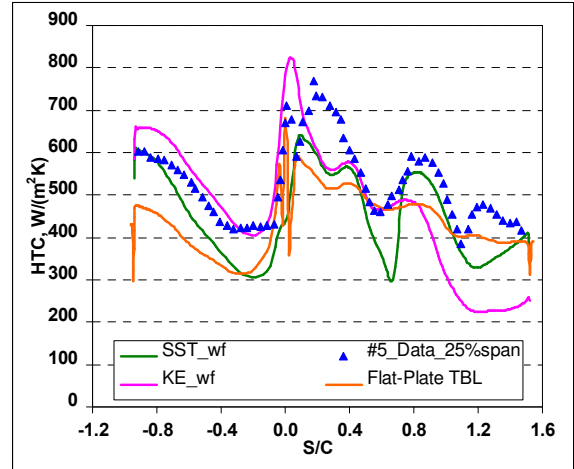


Fig. 13 HTC predicted by k- ϵ and SST with wall-function vs. flat-plate correlation and data at 25% span (Case #5)

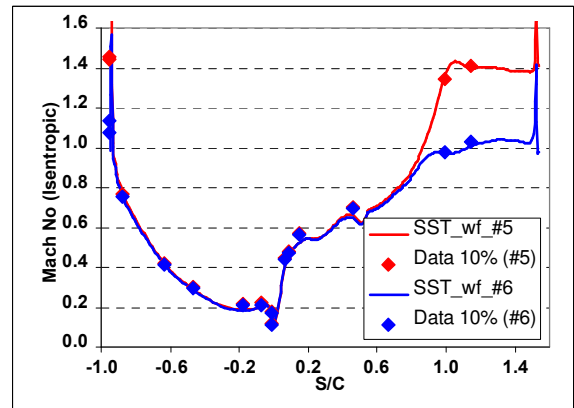


Fig. 14 CFD-predicted (by SST_wf) isentropic Mach number vs. data at 10% span (Case #6 vs. Case #5)

The blade loadings (in terms of isentropic Mach number) at 10% span for Case #5 and #6 are plotted in Fig. 14. The CFD predictions agree with the data very well. The impact of Mach number on the blade HTC (10% span) is presented in Fig. 15, where the HTC drop on the rear suction side has been captured by CFD (SST), although the HTC enhancement by secondary flows has been under-predicted. The rapid drop of HTC starting from around $S/C=0.8$ (suction side) in Fig. 15 for Case #5 appears to be caused by the rapid acceleration there in Case #5, as shown in Fig. 14. As in the measurement, the CFD predictions showed little impact by Mach number on the pressure side.

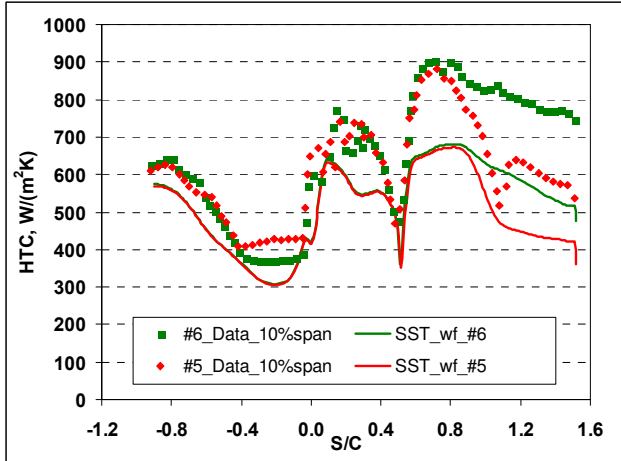


Fig. 15 CFD-predicted HTC (by SST with wall-function) vs. data at 10% span (Case #6 vs. Case #5)

The HTC values from CFD and flat-plate correlation at three locations (10%, 25%, 50% span) are compared to the data in Fig. 16. The flat-plate correlations at all the three sections are almost identical and have been plotted as one thick black line. There is only slight variation at different spans on the pressure side, in the data and predictions. On the suction side, while the flat-plate correlations show no effects of secondary flows, the CFD results largely capture the increasing HTC toward the endwall and follow the wavy distribution.

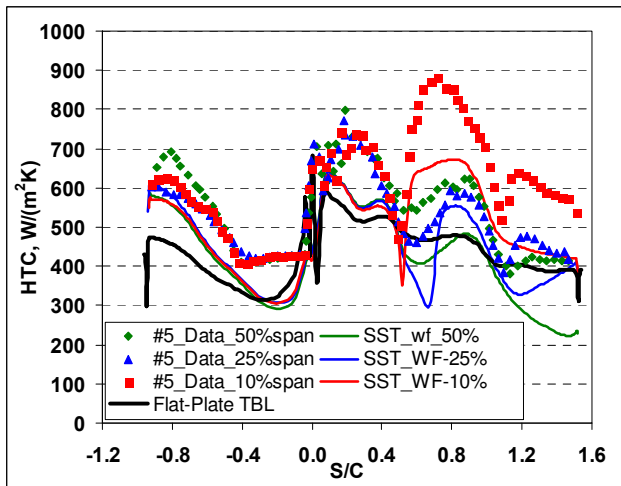


Fig. 16 CFD-predicted (by SST with wall-function) HTC vs. data at three sections (Case #5)

Modeling Migration of Hot Gas

In the above analyses, the inlet T_{t1} was held uniform. To simulate the process of combustor gas passing through turbine stages, additional analysis was conducted with a radial profile of T_{t1} , and adiabatic wall boundary. As shown from the cross-sections (colored by the normalized temperature, ranging from 0.0 at the endwall and 1.0 at the mid-span) in Fig. 17a, the upstream flow has spanwise

gradient of temperature. T_{t1} at mid-span is 50 K higher than that at endwall, i.e., $T_{tmax} - T_{tmin} = 50$ K, with a profile similar to those in industrial turbine engines.

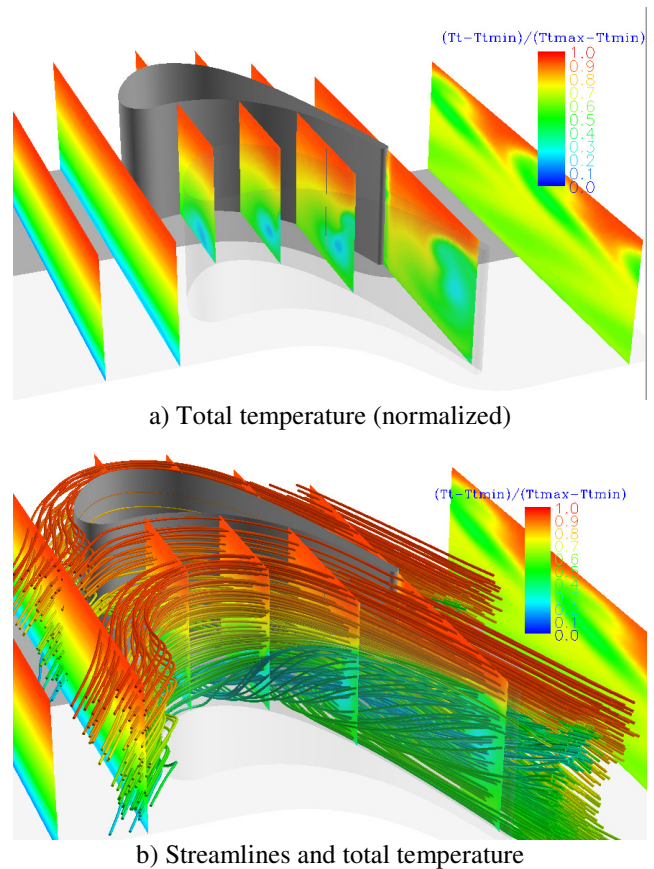


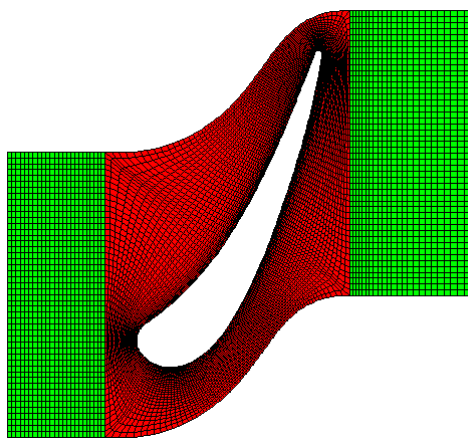
Fig. 17 CFD-predicted (with the SST_wf model) contour plots of total temperature on cross-sections and streamlines

Once inside the passage, T_t contours on the cross-sections start to change, especially near the endwall, due to the development of horse-shoe and passage vortices. The hotter gas, initially near the mid-span, got swept downward near the pressure side towards the endwall, resulting in higher temperature there, while the cooler fluid, initially near the endwall, rolled up into the passage vortex and accumulated near the suction side.

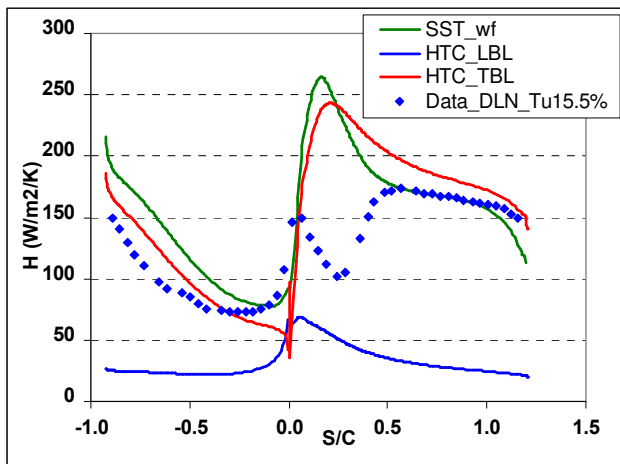
As a result of 3D endwall vortices, the contour at the trailing-edge cross-section deviates greatly from that upstream of the blade, due to the migration and mixing of hot/cold fluid elements. Clearly, such re-distribution of adiabatic temperature due to 3D secondary flows can not be modeled by 1D or 2D codes, but can only be obtained from 3D RANS CFD. The roll-up of passage vortex is shown visually with the streamlines in Fig. 17b. The passage vortex core near the suction side is composed of cooler fluid swept upward from the endwall upstream. Over a large portion of the passage, the pressure side is considerably hotter than the suction side, in agreement with other measurements and simulations [6].

Turbine Nozzle of Ames et al. [23]

CFD analyses were also performed for the turbine nozzle measured by Ames et al. [23] for heat transfer under high inlet turbulence at a typical combustor exit level. The eleven times scale (11x) vane has a true chord of 47.8 cm and an axial chord of 25.0 cm, with the air exit angle of 73.4 degrees. At the inlet turbulence of 15.5% and exit Reynolds number (based on true chord) of 2×10^6 , the predictions from CFD and the flat-plate laminar and turbulent boundary layer correlations are shown in Fig. 18. On the pressure side ($S/C < 0$), the data (slightly lower than the TBL correlation) indicates the boundary layer is still transitional and not fully turbulent. Because of the wall-function and log-law, the SST-wf solution is higher than the data.



a) CFD mesh



b) Predicted HTC vs. Data

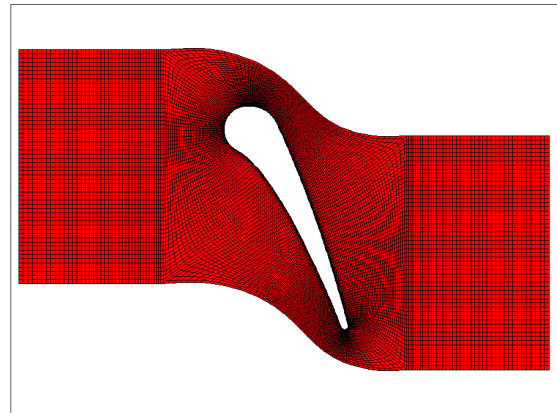
Fig. 18 CFD-predicted HTC (by the SST model and wall function) on the nozzle [23] vs. the flat-plate laminar and turbulent boundary layer correlations and test data

On the suction side, there is a clearly quasi-laminar and transitional zones starting from the leading edge ($S/C=0$) to about $S/C = 0.5$. It is in this front region that the current SST model with wall-function shows a large

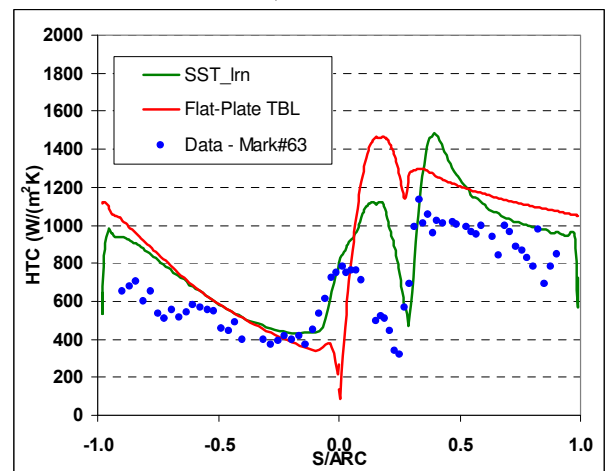
discrepancy from the data, as does the flat-plate TBL correlation. However, on typical turbine stage 1 nozzles, there are film holes near the leading edge, and the boundary layer is most likely triggered by the film jets to become fully turbulent right away. Hence, the absence of transition modeling with the log-law wall functions may not cause significant discrepancy for film-cooled airfoils.

NASA Turbine Nozzle MarkII (Hylton et al. [24])

Another turbine nozzle analyzed was the MarkII airfoil measured in 1980's by Hylton et al. [24]. Under an inlet turbulence intensity of 8.3% and Reynolds number of 10^6 (exit velocity and chord length), the CFD result from the SST model with low-Reynolds-number damping functions is shown in Fig. 19. On the pressure side, the SST solution agrees well with the data and the flat-plate TBL correlation. On the suction, there is again a short zone where the flow is quasi-laminar and transitional ($S/C = 0$ to 0.3). With the LRN damping function, the SST model is able to simulate the flow transition by some degree.



a) CFD mesh



b) HTC (ARC = surface arc length)

Fig. 19 CFD-predicted HTC (by the low-Reynolds-number SST model) on NASA turbine nozzle (MarkII) vs. the flat-plate TBL correlation and test data

CONCLUSIONS

3D RANS analyses have been conducted to predict HTC on the blade and endwall in a NASA turbine rotor passage with strong secondary flow effects. The CFD results for the mid-span HTC of two other airfoils were also presented. The effects of secondary flow vortices, Reynolds number, exit Mach number on the gas-side heat transfer have been examined. From the results and discussion, the following conclusions can be drawn:

Comparisons with test data indicate 3D RANS can be used as a predictor for turbine gas-side HTC on the entire airfoil and endwall, with many benefits over the current tools based on correlations and 2D boundary layer codes.

3D CFD predictions have largely captured elevated HTC on the endwall and blade surface nearby caused by the secondary flow vortices, in agreement with test data and flow physics.

3D CFD predictions of HTC near the mid-span agree favorably with the data (for cases with early transition) and have accuracy comparable with the flat-plate correlations.

For the SST solutions, the log-law wall-function approach was found to be comparable to the low-Reynolds-number treatment. The wall-function provides much reduced sensitivity to inlet turbulence level for the k- ϵ model, in addition to the saving in mesh count.

The SST model has shown better accuracy than the k- ϵ , realizable k- ϵ and V2F models for predicting the heat transfer enhancement on the blade and endwall due to the secondary flow vortices.

By modeling the strong effects of secondary flow vortices, 3D RANS captures the migration of hot gas through the passage, hence providing more accurate local values of adiabatic temperature.

3D RANS CFD predictions should help to achieve improved cooling schemes in the challenging endwall regions and reduce possible "hot spots". Further investigations are needed for film cooling, unsteady effects and conjugate heat transfer modeling.

ACKNOWLEDGEMENTS

We would like to thank Dr. P. Giel and Dr. F. Ames for providing the data from their measurements. We thank Solar Turbines Incorporated for granting permission to publish this work. We are grateful to H. Nasir and M. Okpara for the assistance in generating the flat-plate correlations and other Solar coworkers for many useful discussions.

NOMENCLATURE

C, C_x = airfoil chord length, axial chord length [m]
 HTC (H) = heat transfer coefficient, [W/m²/K]
 $HTC_1 = \dot{Q}_w / (T_{t1} - T_w)$, $HTC_2 = \dot{Q}_w / (T_{aw} - T_w)$
 k = turbulent kinetic energy [m²/s²]
 K = thermal conductivity [W/m/K]
 L_k = turbulence length scale, $0.8165k^{1.5}/\epsilon$

L_t = turbulence length scale used in STAR-CD [m]
 $L_t = C_\mu^{3/4} k^{1.5} / \epsilon$, or $L_t = 0.164 k^{1.5} / \epsilon$
 L_x = longitudinal integral scale [m]
 M (Ma) = Mach number
 Nu = Nusselt number ($Nu = H^*S/K$)
 P_{t1} = inlet total pressure [Pa, or bar (10^5 Pa)]
 P = static pressure [Pa, or bar]
 Pr = Prandtl number
 PS / SS = Pressure side / Suction side
 \dot{Q}_w = wall heat flux [W/m²]
 r_c = recovery factor, $Pr^{1/3}$
 Re_S = Reynolds number based on S and U,
 $Re_s = U S / \nu$
 S = surface distance from airfoil leading edge (S/C: <0 on pressure side, >0 on suction side)
 St = Stanton number ($H/\rho U C_p, C_p =$ specific heat)
 TBL = turbulent boundary layer
 T_{t1} = inlet total temperature [K]
 T_{aw} = adiabatic wall temperature,

$$T_{aw} = T_t \left(\frac{1 + r_c \cdot \frac{\gamma - 1}{2} Ma^2}{1 + \frac{\gamma - 1}{2} Ma^2} \right)$$

 Tu = turbulence intensity, $\sqrt{2/3 k} / U$
 U = freestream velocity or local velocity [m/s]
 U_τ = friction velocity [m/s] ($\sqrt{\tau_w / \rho}$, $\tau_w =$ skin friction)
 y^+ = non-dimensional distance from wall,
 $y^+ = U_\tau y / \nu$
 ϵ = dissipation rate of turbulent energy [m²/s³]
 μ = molecular dynamic viscosity [Pa · s]
 ν = kinematic viscosity (μ/ρ) [m²/s]
 μ_t = turbulent eddy viscosity [Pa · s], $\rho \nu_t$
 ρ = density
Subscripts
 1, 2 = cascade inlet, exit
 in / ex = inlet / exit
 s = streamwise/curvilinear
 t = total (stagnation) condition
 w = wall property

REFERENCES

- [1] Simon T. W., and Piggush, J. D., 2006, "Turbine Endwall Aerodynamics and Heat Transfer," *AIAA J. of Propulsion and Power*, Vol. 22, No. 2, pp. 301-312.
- [2] Goldstein, R.J., and Spores, R. A., 1988, "Turbulent Transport on the Endwall in the Region Between Adjacent Turbine Blades," *ASME J. of Heat Transfer*, Vol. 110, pp. 862-869.
- [3] Giel, P. W., Thurman, D. R., Van Fossen, G. J., Hippensteele, S. A., Boyle, R. J., 1998, "Endwall Heat Transfer Measurements in a Transonic Turbine Cascade," *ASME J. of Turbomachinery*, vol. 120, pp. 305-313.

- [4] Giel, P. W., Van Fossen, G. J., Boyle, R. J., Thurman, D. R., and Civinskas, K. C., 1999, "Blade Heat Transfer Measurements and Predictions in a Transonic Turbine Cascade," ASME Paper 99-GT-125.
- [5] Radomsky, R.A., and Thole, K. A., 2000, "High Freestream Turbulence Effects on Endwall Heat Transfer For a Gas Turbine Stator Vane," ASME paper 2000-GT-0201.
- [6] Dunn, M. G., 2001, "Convective Heat Transfer and Aerodynamics in Axial Flow Turbines," ASME *J. of Turbomachinery*, 123, pp. 637-686.
- [7] Medic, G., and Durbin, P. A., 2002, "Toward Improved Prediction of Heat Transfer on Turbine Blades," ASME *J. of Turbomachinery*, 124, pp. 187 - 192.
- [8] Hermanson, K., Kern, S., Picker, G., and Parneix, S., 2002, "Predictions of External Heat Transfer for Turbine Vanes and Blades with Secondary Flowfields," ASME paper GT2002-30206.
- [9] Ameri, A. A., and Ajmani, K., 2004, "Evaluation of Predicted Heat Transfer on a Transonic Blade Using v2-f models," ASME paper GT2004-53572.
- [10] Tolpadi, A. K., Tallman, J. A., El-Gabry, L., 2005, "Turbine Airfoil Heat Transfer Predictions Using CFD", ASME GT2005-68051.
- [11] Pecnik, R., Pieringer, P. and Sanz, W., 2005, "Numerical Investigation of the Secondary Flow of a Transonic Turbine Stage Using Various Turbulence Closures," ASME paper GT2005-68754.
- [12] Mansour, M. L., Hosseini, K. M., Liu, J., S., and Goswami, S., 2006, "Assessment of the Impact of Laminar-Turbulent Transition on the Accuracy of Heat Transfer Coefficient Prediction in High Pressure Turbines," ASME paper GT2006-90273.
- [13] Tallman, J. A., Haldeman, C. W., Dunn, M. G., Tolpadi, A. K., Bergholz, R. F., 2009, "Heat Transfer Measurements and Predictions for a Modern, High-Pressure, Transonic Turbine, Including Endwalls," ASME *J. of Turbomachinery*, Vol. 131, pp. 021001: 1-14 (GT2006-90927).
- [14] Kays, W. M., Crawford, M. E., and Weigand, B., 2004, *Convective Heat and Mass Transfer*, McGraw-Hill Book Company, New York.
- [15] Praisner, T. J., and Clark, J. P., 2007, "Predicting Transition in Turbomachinery - Part I: A Review and New Model Development", ASME *J. of Turbomachinery*, 129, pp. 1-13.
- [16] Luo, J., and Razinsky, E., 2008, "Prediction of Heat Transfer and Flow Transition on Transonic Turbine Airfoils Under High Freestream Turbulence", ASME GT2008-50868.
- [17] Kusterer, K., Hagedorn, T., Bohn, D., Sugimoto, T., Tanaka, R., 2005, "Improvement of a Film-Cooled Blade by Application of the Conjugate Calculation Technique," ASME GT2005-68555.
- [18] Luo, J., and Razinsky, E., 2007, "Conjugate Heat Transfer Analysis of a Cooled Turbine Vane Using the V2F Turbulence Model," ASME *J. of Turbomachinery*, 129, pp. 773-781 (GT2006-91109).
- [19] He, L., Oldfield, M. L. G., 2009, "Unsteady Conjugate Heat Transfer Modelling," ASME GT2009-59174, Orlando, FL.
- [20] STAR-CD Version 4.10 - methodology, 2009, CD-adapco Group, New York / London.
- [21] Durbin, P. A., 2009, "Limiters and Wall Treatments in Applied Turbulence Modeling", Fluid Dynamics Research 41.
- [22] Levchenya, A. M., and Smirnov, E. M., 2007, CFD-Analysis of 3D Flow Structure and Endwall Heat Transfer in a Transonic Turbine Blade Cascade: Effects Of Grid Refinement", West-East High Speed Flow Field Conference, Nov., Moscow, Russia.
- [23] Ames, F. E., Wang, C., and Barbot, P.A., 2002, "Measurement And Prediction Of The Influence Of Catalytic And Dry Low Nox Combustor Turbulence On Vane Surface Heat Transfer", ASME paper GT2002-30524.
- [24] Hylton, L.D., Milhec, M.S., Turner, E.R., Nealy, D.A., and York, R.E., 1983, "Analytical and Experimental Evaluation of the Heat Transfer Distribution over the Surface of Turbine Vanes", NASA CR 168015.
- [25] Hinze, J. O., 1975, *Turbulence*, McGraw-Hill Book Company, Inc., New York.
- [26] Ames, F. E., 1994, "Experimental Study of Vane Heat Transfer and Aerodynamics at Elevated Levels of Turbulence," NASA CR 4633.
- [27] Horlock, J. H., Denton, J. D., 2005, "A Review Of Some Early Design Practice Using Computational Fluid Dynamics and A Current Perspective," ASME *J. of Turbomachinery*, Vol. 127, pp. 5-13 (2003-GT-38973).